Supplementary figures and tables

S1: Model vegetation and aerosol fields.

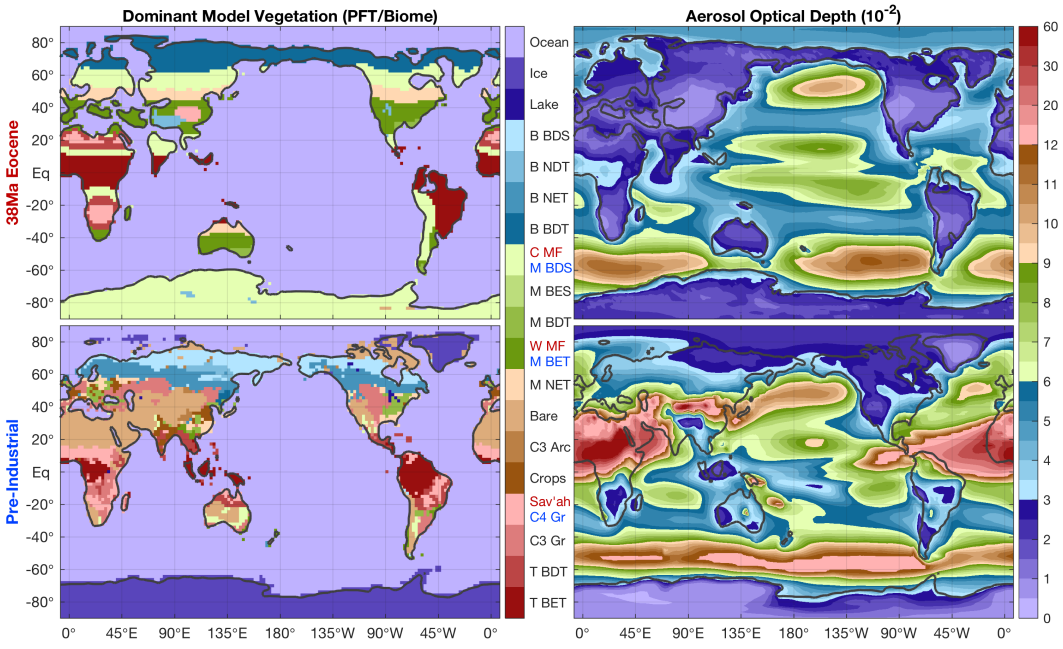

Figure S1. Model vegetation (left) and aerosol optical depth (right) used in both 38Ma cases (top) and the pre-industrial reference (bottom). Vegetation is indicated as either the biome (38Ma) or dominant plant functional type (PFT; pre-industrial), where many considered biomes consist of a single PFT (see also Table S1). In the PFT list, the main classes are B for boreal, M for temperate and T for tropical. A further distinction is made between (left to right) B: broadleaf / N: needleleaf; D: deciduous / E: evergreen; S: shrub / T: tree. C3/C4 are grasses, with C3 divided into arctic (Arc) and non-arctic. Three specific biomes are used in the 38Ma cases (indicated in red); C/W MF which stands for cool/warm mixed forest, consisting of different mixes of temperate trees and Savannah.

PFT / Biome	T BET	T BDT	C3 Grass	Bare	M NET	M BET	M BDT	B BDT	B NET	B NDT
Land ice				1						
C NDT										1
C NET									1	
C BDT							0.25	0.25	0.5	
C MF					0.5	0.5				
W BDT							1			
W MF					0.34	0.33	0.33			
W NET					1					
Desert				1						
Svannah		0.5	0.5							
T BDT		1								
T BET	1									

Table S1. Used relations between biomes and fractions of CLM4 plant functional types (PFTs). Note that only the biomes and PFTs used in the Eocene simulations presented here are shown. In the list of biomes, T denotes *tropical*, W *warm* and C *cool*. See also Figure S1 for an overview of PFT names.

S2: Time series and patterns of ideal age tracers.

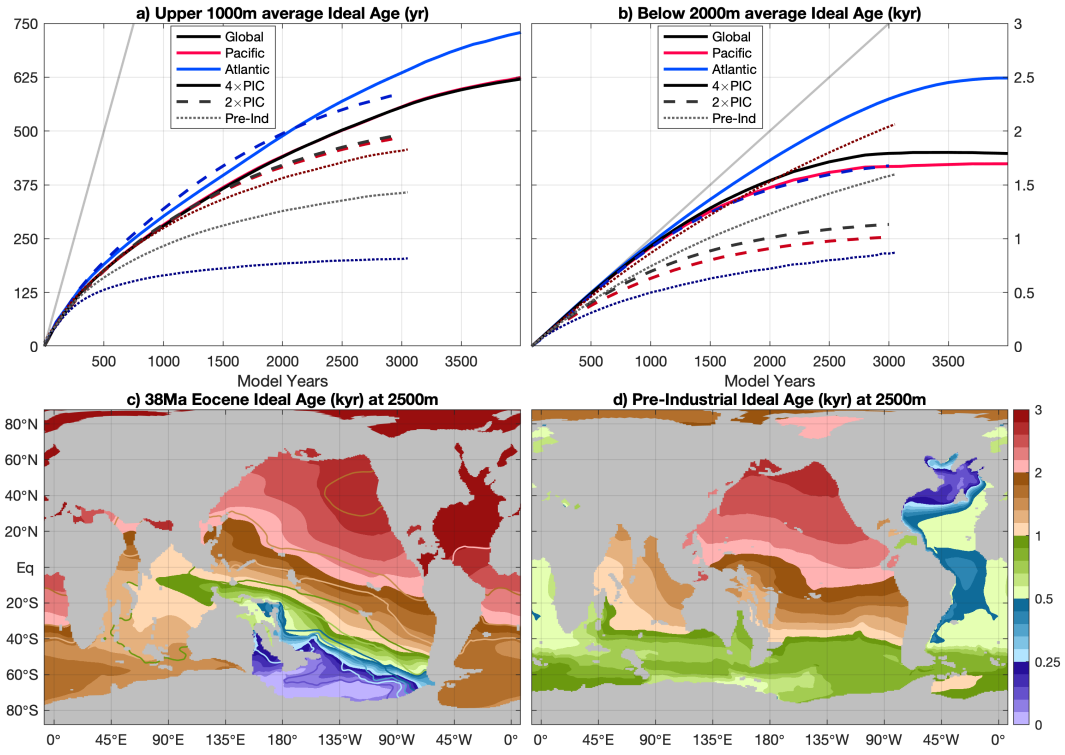

Figure S2. Time series of **a)** upper 1km and **b)** below 2km volume-weighted average ideal age tracers for Pre-industrial (dotted), 38Ma 2×PIC (dashed) and 4×PIC (solid) spin-up simulations. Averages are shown globally (black) and for both the Pacific (red) and Atlantic (blue) ocean basins separately. **c)** 38Ma and **d)** pre-industrial horizontal distributions of ideal age tracers at 2500m depth for the end of each model simulation. Colour shading in c) shows the ideal age of 4×PIC, while contours do so for the 2×PIC case (using the same colourmap shown to the right).

S3: Time series of Southern Ocean gateways and meridional overturning strength.

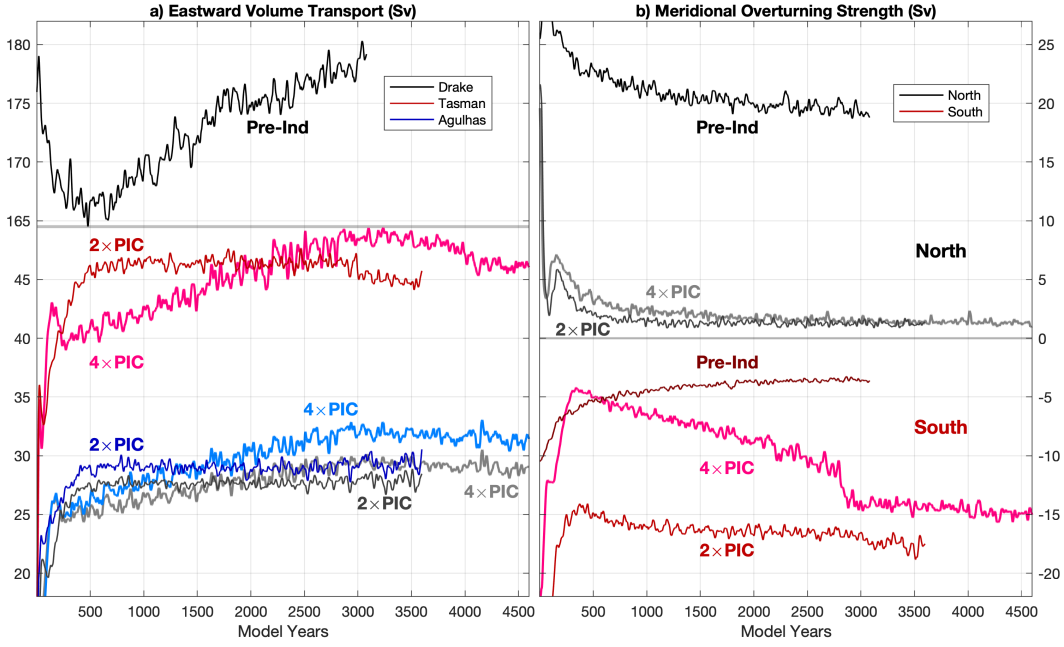

Figure S3. Time series of **a)** Southern Ocean Gateway volume transports and **b)** maximum global meridional overturning for both 2×PIC (dashed), 4×PIC (solid) Eocene and pre-industrial (dotted) spin-up simulations. Transports through three (one for pre-industrial) north-south transects in the Southern Ocean are considered: Drake Passage (black, 65°W), Tasmanian Gateway (red, 150°E) and Agulhas (blue, 25°E), with positive values indicating eastward flow.

S4: Annual mean oceanic fields of the pre-industrial reference.

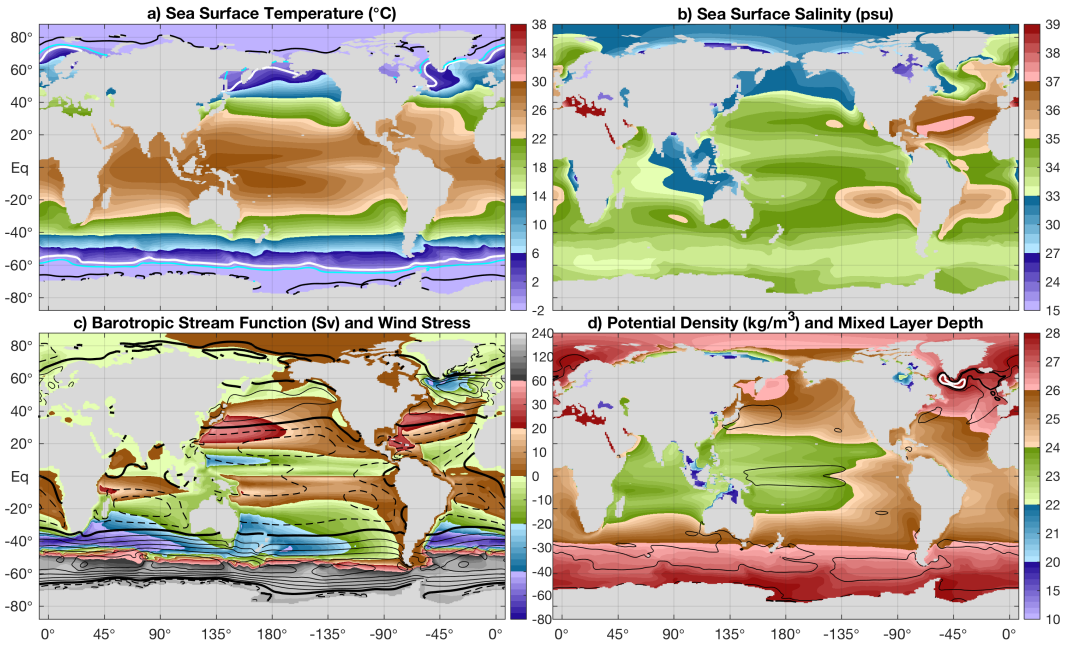

Figure S4. Annual mean for the pre-industrial reference with **a)** sea surface temperature and **b)** salinity, **c)** barotropic stream function (positive for clockwise flow) and zonal wind stress (contours every $4{\cdot}10^{-2}$Pa, solid positive and dashed negative, thick line at 0Pa), and **d)** upper 200m average potential density and mixed layer depth (contours at 100m and 250m, thick white line at 500m). Note the adjusted scale in c) compared to Figures 3 and S5), to show the much higher values in the Southern Ocean compared to 38Ma cases. Contours in a) show annual mean sea ice fraction at 15% (white), 50% (cyan) and 90% (black).

S5: Annual mean oceanic fields of the 38Ma 2×PIC case.

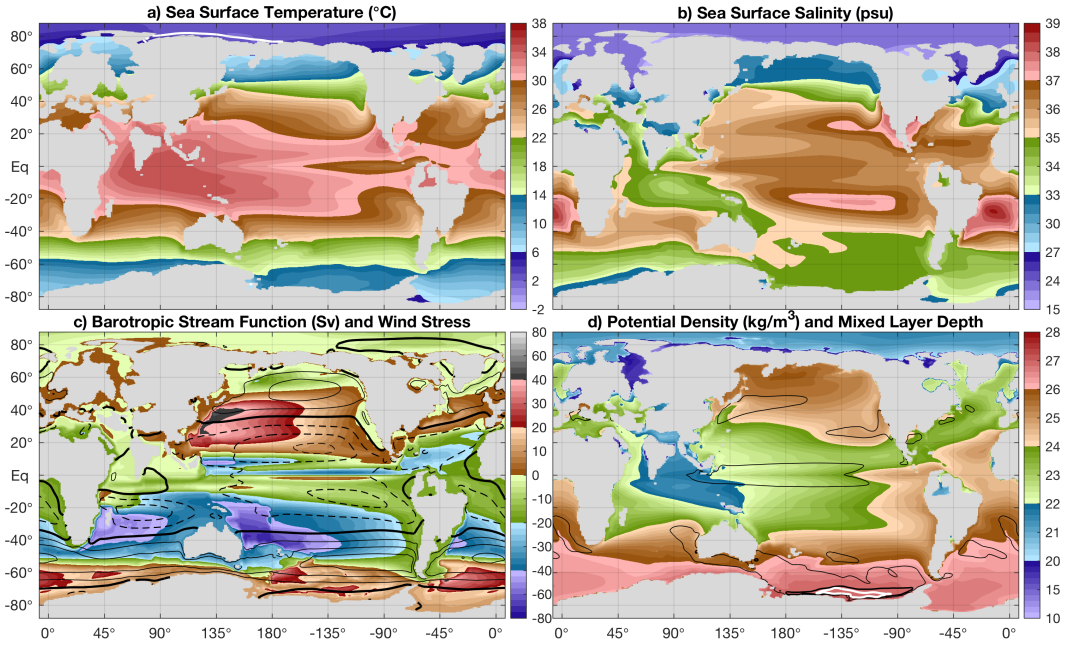

Figure S5. Annual mean for the 38Ma 2×PIC simulation with **a)** sea surface temperature and **b)** salinity, **c)** barotropic stream function (positive for clockwise flow) and zonal wind stress (contours every $4{\cdot}10^{-2}$Pa, solid positive and dashed negative, thick line at 0Pa), and **d)** upper 200m average potential density and mixed layer depth (contours at 100m and 250m, thick white line at 500m). The white contour in a) shows annual mean sea ice fraction at 15% (white).

S6: Annual mean atmospheric fields of the pre-industrial reference.

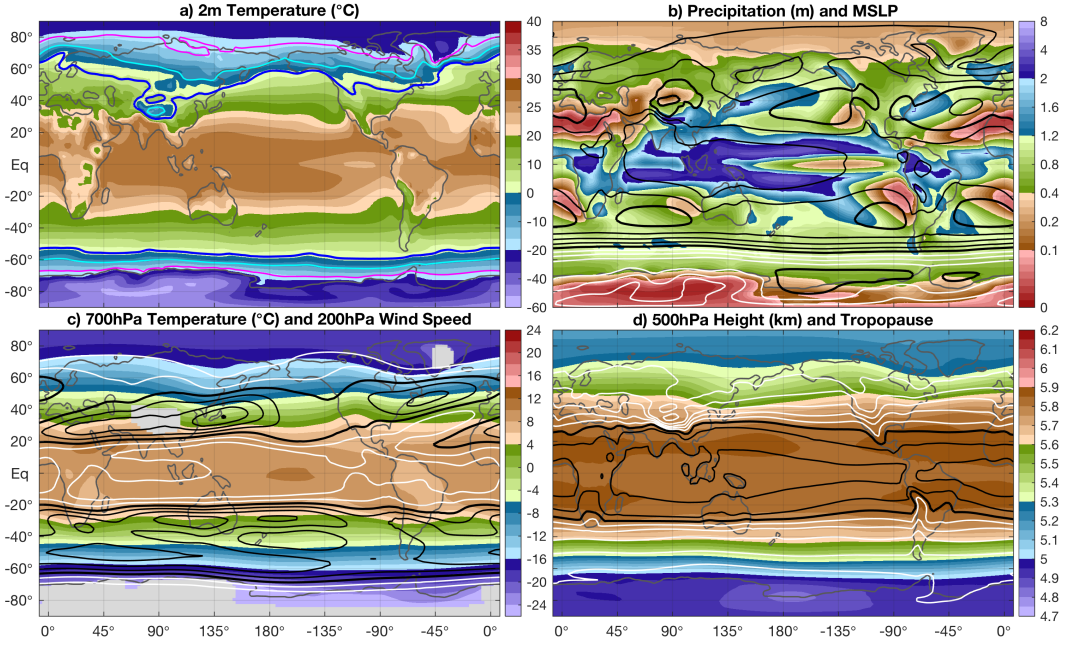

Figure S6. Annual mean for the pre-industrial reference with **a)** near surface (2m) air temperature (shading) and average min/max temperature (contours; blue: T_{min} <0°C, cyan: T_{min} <-10°C, magenta: T_{min} <-20°C), **b)** precipitation (shading) and mean sea level pressure (MSLP; contours every 5hPa, thick black lines every 20hPa, ≥1000hPa in black and <1000hPa in white), **c)** 700hPa temperature (shading) and 200hPa wind speed (contours every 5m/s starting at 10m/s; white for <20m/s and black for ≥20m/s, thick black lines every 20m/s), and **d)** 500hPa geopotential height (shading) and tropopause height (contours every 1km; white for <15km and black for ≥15km, thick black line at 15km).

S7: Annual mean atmospheric fields of the 38Ma 2×PIC case.

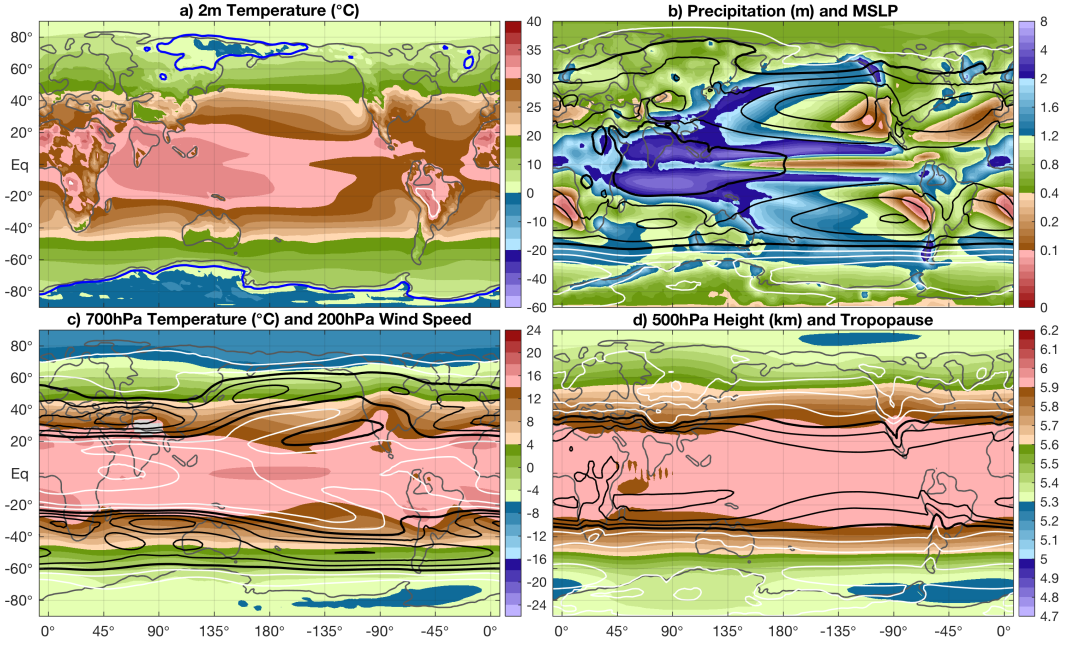

Figure S7. Annual mean for the 38Ma 2×PIC simulation with **a)** near surface (2m) air temperature (shading) and average min/max temperature (contours; blue: T_{min} <0°C and white: T_{max} >40°C), **b)** precipitation (shading) and mean sea level pressure (MSLP; contours every 5hPa, thick black lines every 20hPa, ≥1000hPa in black and <1000hPa in white), **c)** 700hPa temperature (shading) and 200hPa wind speed (contours every 5m/s starting at 10m/s; white for <20m/s and black for ≥20m/s, thick black lines every 20m/s), and **d)** 500hPa geopotential height (shading) and tropopause height (contours every 1km; white for <15km and black for ≥15km, thick black line at 15km).

S8: Seasonal mean oceanic fields of the 38Ma 4×PIC case.

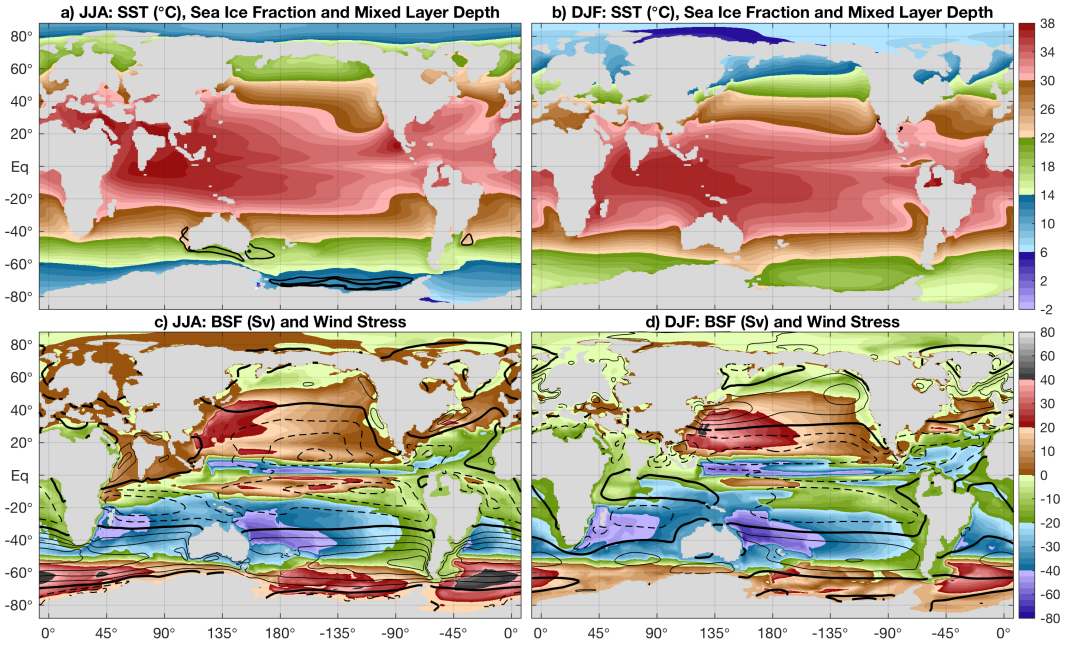

Figure S8. 38Ma 4×PIC **a)** June-July-August and **b)** December-January-February mean sea surface temperature (shading) and mixed layer depth (contour lines at 100m and 200m, thick line at 500m). **c)** and **d)** Similar to a) and b), but for the barotropic stream function and zonal wind stress (contours every $5{\cdot}10^{-2}$Pa; solid positive and dashed negative, thick line at 0Pa). White contours in a) and b) show sea ice fraction at 15% (cyan) in August and February, respectively (but are nearly non-existent).

S9: Seasonal mean atmospheric fields of the 38Ma 4×PIC case.

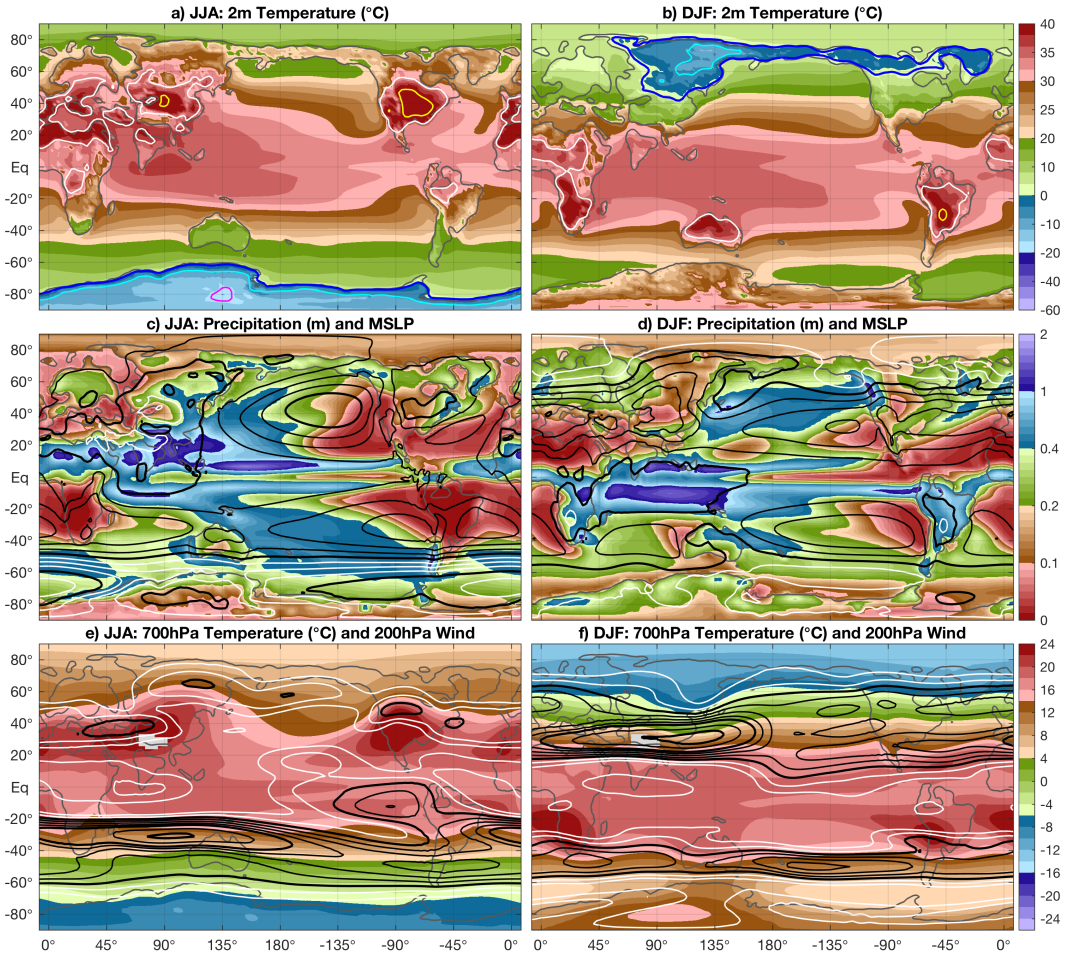

Figure S9. 38Ma 4×PIC **a)** June-July-August and **b)** December-January-February mean 2m air temperature (shading) and min/max temperature (contours; magenta: $T_{min} < 0^{\circ}$C, cyan: $T_{min} < -10^{\circ}$C, blue: $T_{min} < -20^{\circ}$C, white: $T_{max} > 40^{\circ}$C and yellow: $T_{max} > 50^{\circ}$C), **c)** and **d)** similar to a) and b) for total precipitation (shading) and mean sea level pressure (contours every 5hPa, thick black lines every 20hPa, ≥1000hPa in black and <1000hPa in white), and **e)** and **f)** for 700hPa temperature (shading) and 200hPa wind speed (contours every 5m/s starting at 10m/s; white for <20m/s and black for >20m/s, thick black lines every 20m/s).

1220

S10: Zonal average SST of the 38Ma 2×PIC case and 38–34 Ma proxies.

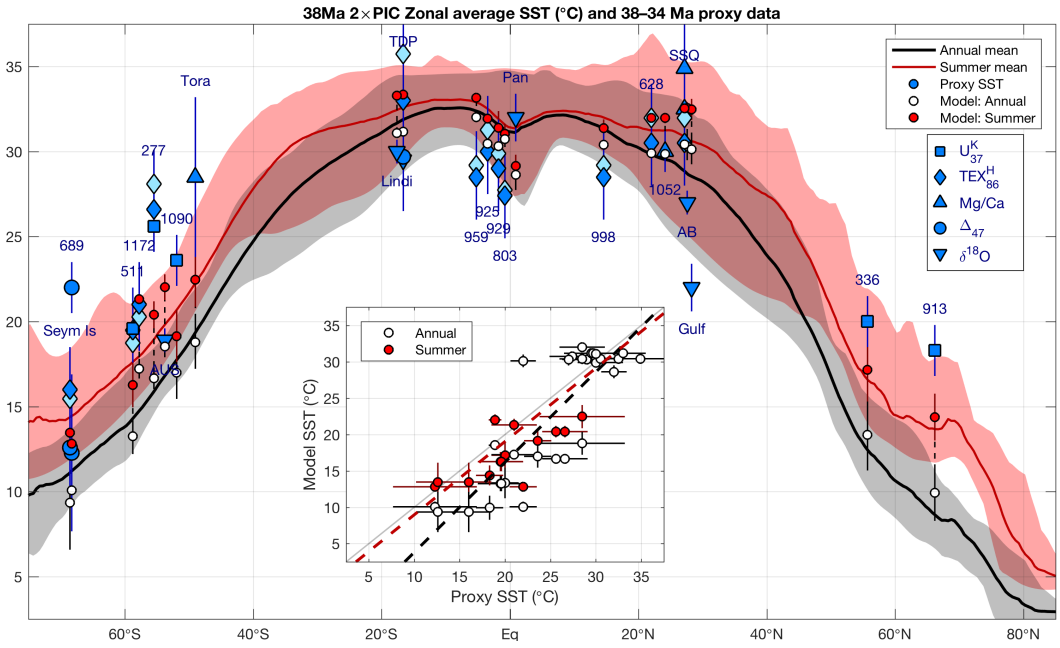

Figure S10. Zonally averaged annual mean (black) and summer mean (red) SST, shaded regions showing zonal spread for the 38Ma 2×PIC case. Blue markers indicate SST proxy estimates (light blue: linear, dark: log calibration from Kim et al. 2008 for TEX^H_{86}), whereas white (annual) and red (summer) circles depict model values at the corresponding 38Ma locations. Error bars represent proxy calibration errors and the model spatial variation within a $4^\circ \times 4^\circ$ box. The inset shows a scatter plot of model versus proxy SST, with a linear fit using annual mean (black) or summer mean (red; only outside of the tropics) model values.

S11: Zonal average near surface air temperature of the 38Ma 4×PIC case and 42–38 Ma proxies.

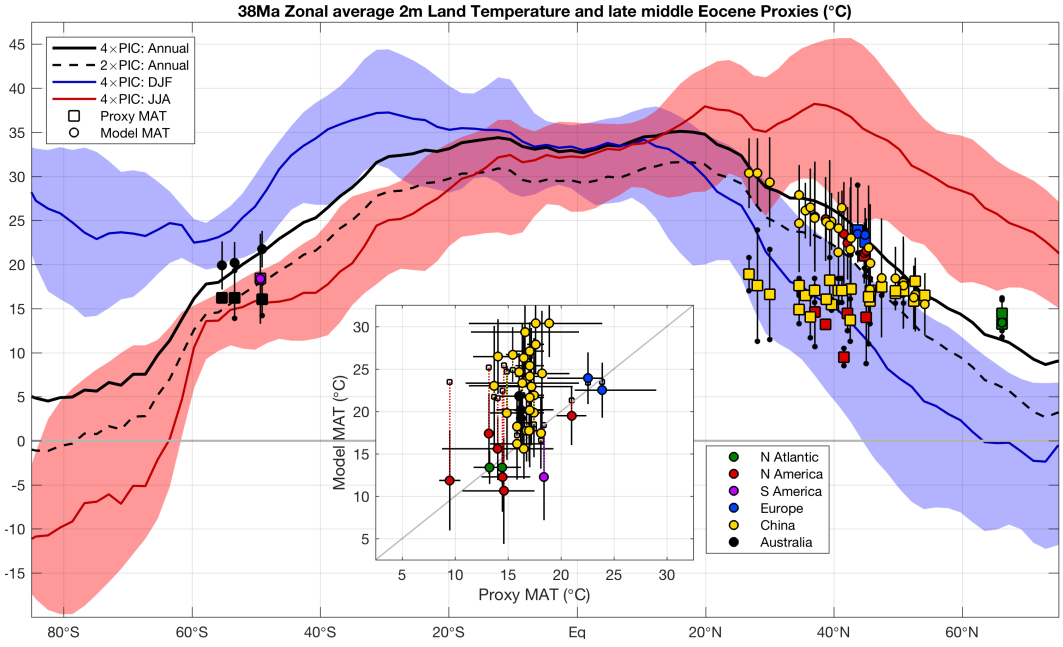

Figure S11. Zonally averaged annual mean (black), December–February (blue) and June–August (red) near surface air temperature (land-only) for the 38Ma 2×PIC case (solid line; dashed: 4×PIC). Red and blue shading indicate zonal variability of the according seasonal means. Markers show late middle Eocene proxy estimates (squares) and corresponding model annual mean (circles), colour coded for their respective region. Error bars (black dots) are indicative of the spread at each site (proxies) or spatial variation in a $5^\circ \times 4^\circ$ box (model). The inset shows a scatter plot of model versus proxy air temperatures, the former being corrected for differences in model and reconstructed topography (uncorrected: small squares).

S12: Zonal average near surface air temperature of the 38Ma 2×PIC case and 38–34 Ma proxies.

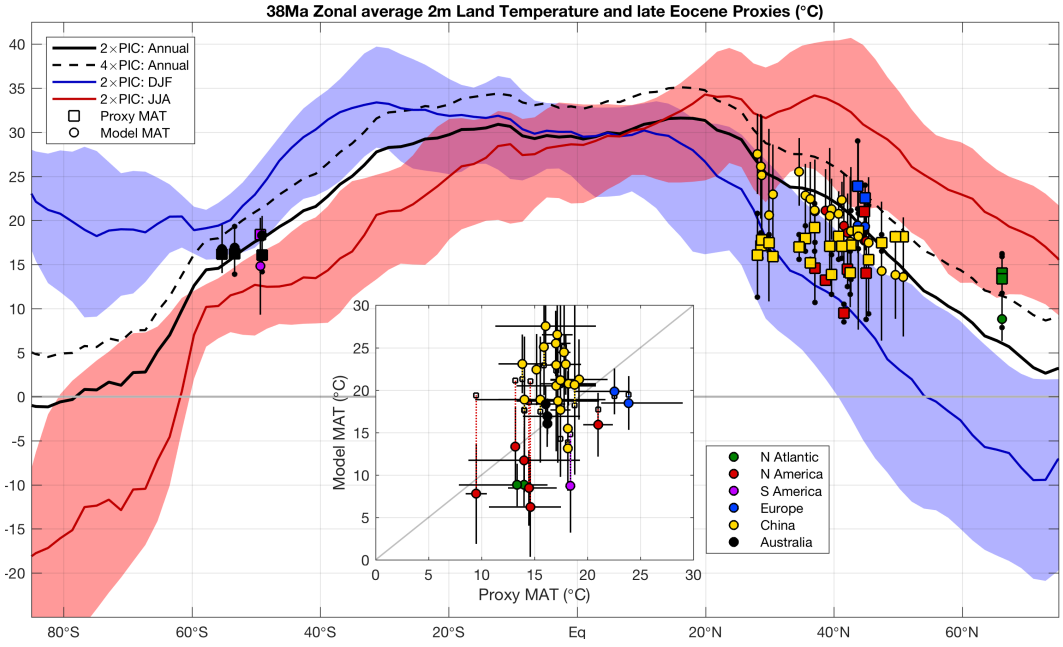

Figure S12. Zonally averaged annual mean (black), December–February (blue) and June–August (red) near surface air temperature (land-only) for the 38Ma 2×PIC case (solid line; dashed: 4×PIC). Red and blue shading indicate zonal variability of the according seasonal means. Markers show late Eocene proxy estimates (squares) and corresponding model annual mean (circles), colour coded for their respective region. Error bars (black dots) are indicative of the spread at each site (proxies) or spatial variation in a 5°×4° box (model). The inset shows a scatter plot of model versus proxy air temperatures, the former being corrected for differences in model and reconstructed topography (uncorrected: small squares).

1225

S13: Comparison of oceanic fields from the 38Ma 4×PIC case and 45Ma 4×CO_2 (GH14).

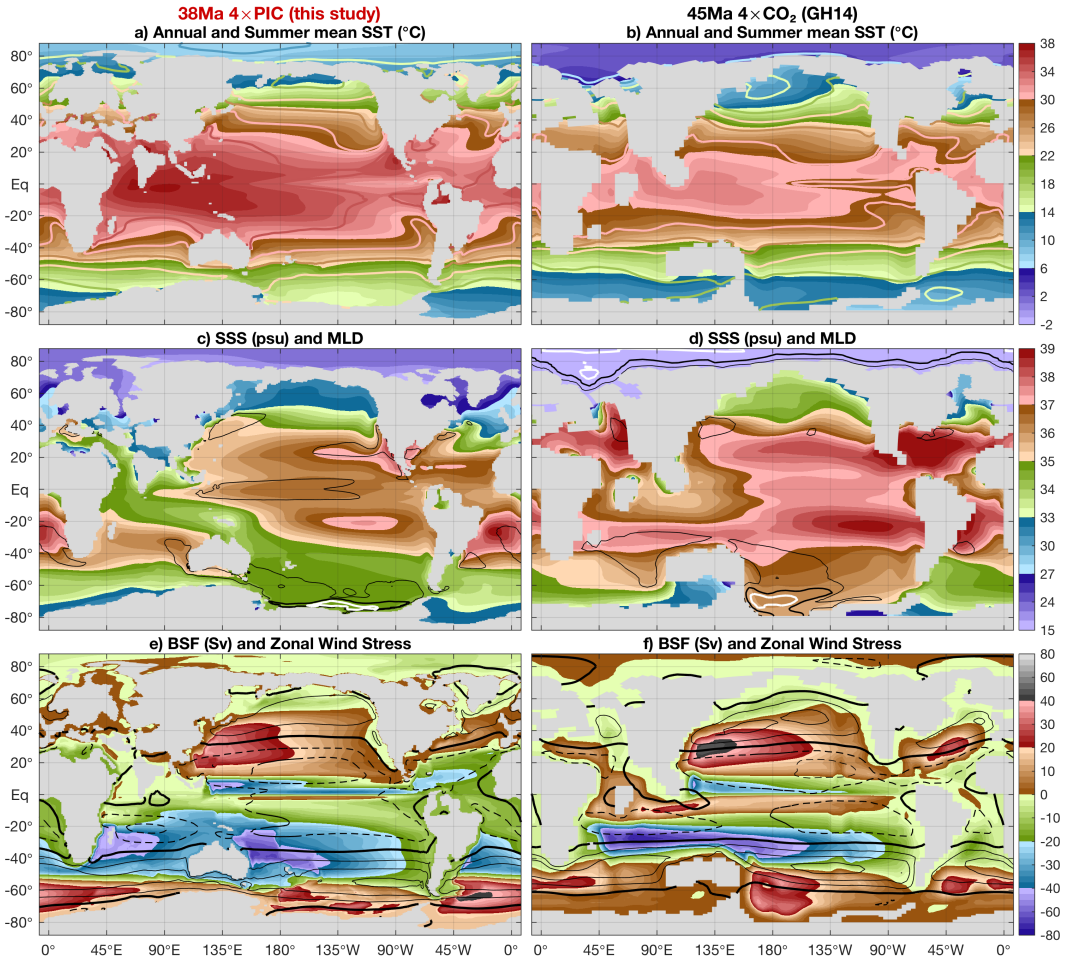

Figure S13. Annual mean (shading) and summer (contours every 4°C) sea surface temperatures for the **a)** 38Ma 4×PIC simulation (this study) and **b)** from Goldner et al. (2014) (GH14) using a 45Ma geography reconstruction and a 4× pre-industrial CO_2 concentration. A similar comparison is made in **c)** and **d)** for sea surface salinity (shading) and mixed layer depth (contour lines at 100m and 200m, thick line at 500m), as well as in **e)** and **f)** for barotropic stream function (shading) and zonal wind stress (contours every $5{\cdot}10^{-2}$Pa; solid positive and dashed negative, thick line at 0Pa). All colour scales and contour intervals meet the same conventions as those used in Figures 3 and S5.

S14: Comparison of atmospheric fields from the 38Ma 4×PIC case and 45Ma 4×CO_2 (GH14).

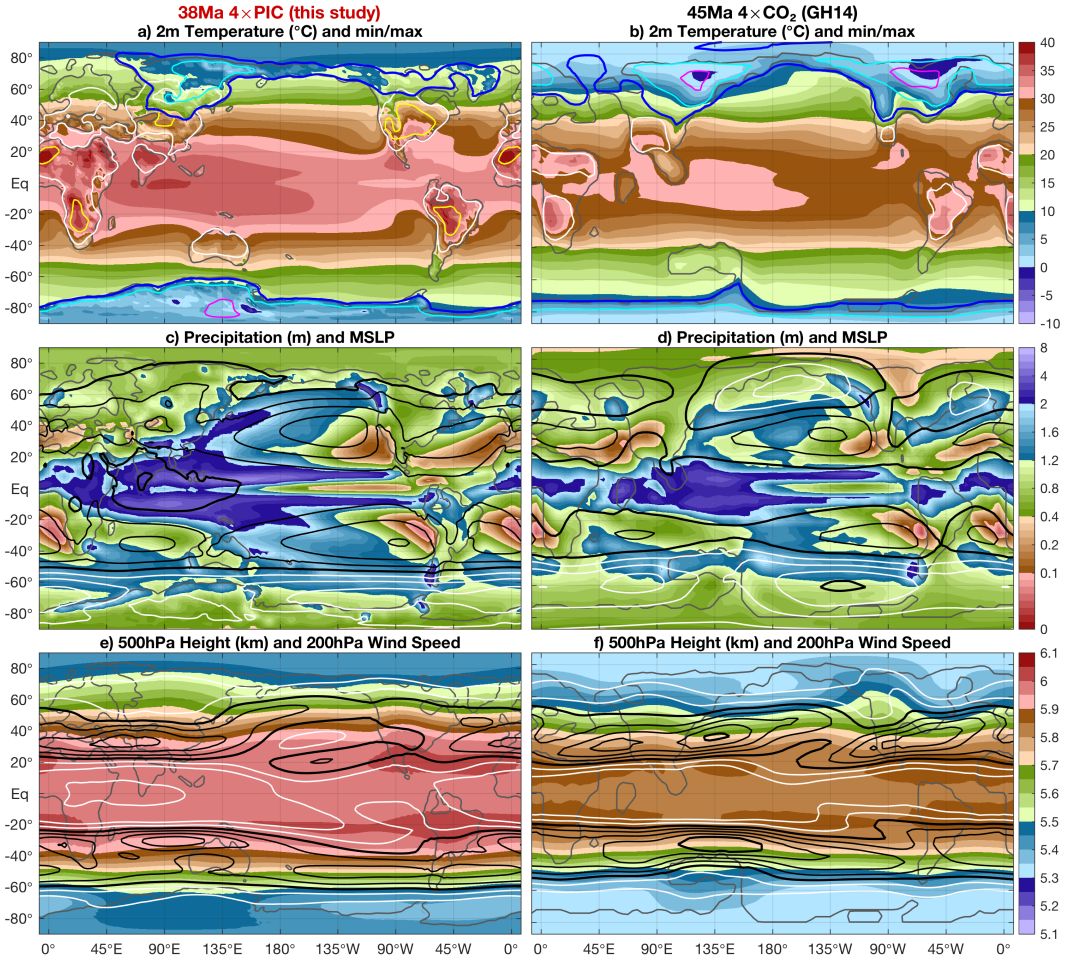

Figure S14. Annual mean (shading), warmest monthly maximum (white: 40°C and yellow: 50°C) and coldest minimum (magenta: 0°C, cyan: -10°C, blue: -20°C) near surface air temperature for the **a)** 38Ma 4×PIC simulation (this study) and **b)** from Goldner et al. (2014) (GH14) using a 45Ma geography and 4× pre-industrial CO_2. A similar comparison is made in **c)** and **d)** for precipitation (shading) and mean sea level pressure (contours every 5hPa, thick black lines every 20hPa, ≤1000hPa in black and >1000hPa in white), as well as in **e)** and **f)** for 500hPa geopotential height (shading) and 200hPa wind speed (contours every 5m/s starting at 10m/s; white for <20m/s and black for >20m/s, thick black lines every 20m/s). All colour scales and contour intervals meet the same conventions as those used in Figures 4 and S7.

S15: Comparison of zonally averaged atmospheric warming patterns.

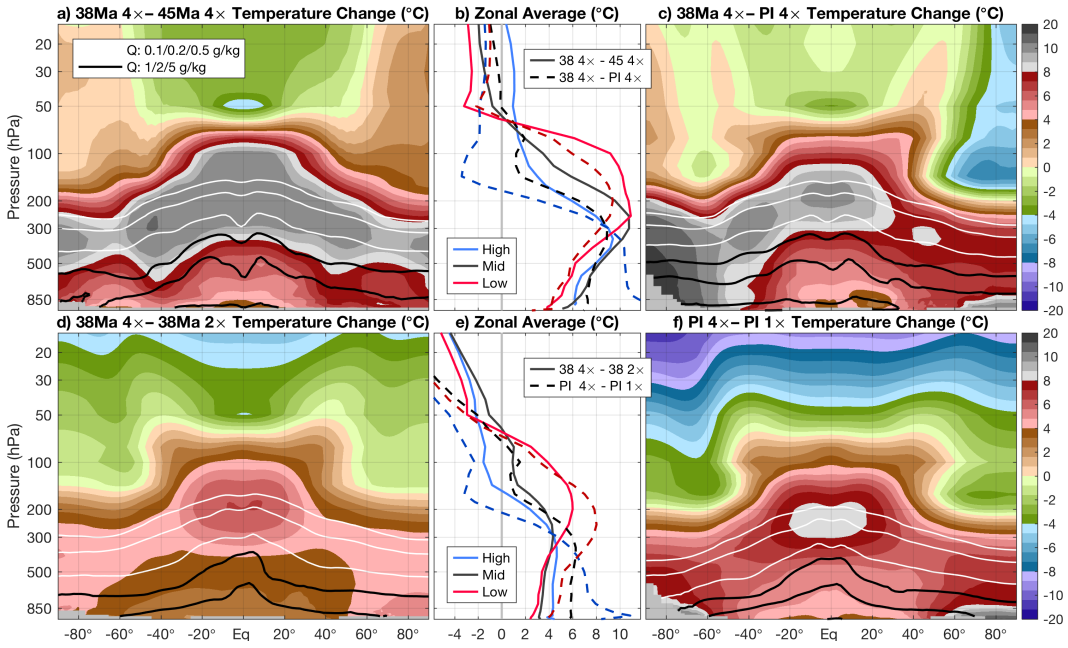

Figure S15. Zonally averaged temperature (shading) and humidity Q (contours; white: <1 g/kg and black: ≥ 1 g/kg) difference for **a)** 38Ma 4×PIC versus 45Ma 4×CO_2 (GH14), **c)** 38Ma 4×PIC versus the pre-industrial reference, **d)** 38Ma 4×PIC versus 38Ma 2×PIC, and **f)** pre-industrial 4×CO_2 versus the pre-industrial reference. Meridionally averaged temperature changes are shown in the **b)** and **e)** for low (0–30°; red), middle (30–60°; black) and high (60–90°; blue) latitudes, respectively (both hemispheres). Solid lines correspond to the pattern shown to the left, dashed lines to the one to the right.

Comparison of globally averaged atmospheric fluxes.

Flux (W/m^2) \ Case	**38 4×−45 4×**	**38 4×−38 2×**	**38 4×−PI 4×**	**PI 4×−PI 1×**
Shortwave$_{surface}$	−0.25	+0.08	+7.49	+4.65
Shortwave$_{top}$	+14.73	+1.66	+9.66	+4.73
Shortwave$_{atmosphere}$	−5.40	−3.02	−4.31	−4.70
Shortwave$_{cloud}$	+13.84	+1.27	+0.21	−0.73
Longwave$_{top}$	−14.67	−1.63	−10.00	−4.55
Longwave$_{atmosphere}$	+22.38	+9.06	+24.93	+14.16
Longwave$_{cloud}$	−6.40	−1.16	+0.35	−0.99

Table S2. Globally averaged flux differences for the four model-model comparison cases shown in Figure S15. All of the flux components are defined such that a positive number (red) means that the specific component has a warming effect, while negative values (blue) induce a cooling. Total fluxes are divided into their shortwave and longwave parts, which are then subdivided into more specific components. *Surface* and *top* denote the respective change in partial radiative balance, while *atmosphere* and *cloud* refer to the respective effect on that balance (i.e. the effect of the clear atmosphere and integrated cloud cover).

S16: Model response to instant 4×CO_2 from the pre-industrial reference.

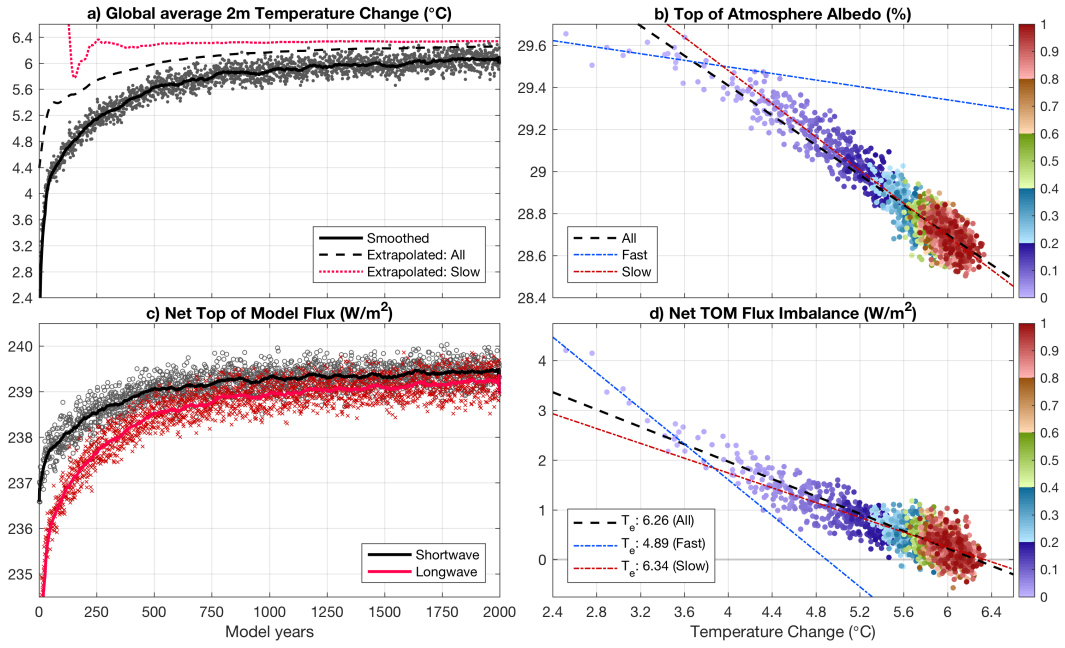

Figure S16. Modelled response after an instant quadrupling of atmospheric CO_2, starting from the equilibrated state of the pre-industrial reference. **a)** Annual mean globally averaged near surface air temperature change (dots; thick line: 50-year running mean) with the dashed black line showing the extrapolated response to that point (red: excluding the first 100 years, i.e. 'slow' response). **b)** Top of the atmosphere albedo: annual (markers; coloured to normalised model time) and linear interpolation (black: all, blue: using only the first 20 years and red: excluding the first 100 years). **c)** Top of model net shortwave (black) and longwave flux (red): yearly (markers) and with 50-year running mean (lines). **d)** Top of model flux imbalance (shortwave - longwave, see c)) versus globally averaged temperature change (from the pre-industrial reference): annual (markers) and interpolated (lines; as in b)), with extrapolated values of global average temperature given for the different methods considered here.

S17: Fast response to instant 4×CO_2 and radiative forcing.

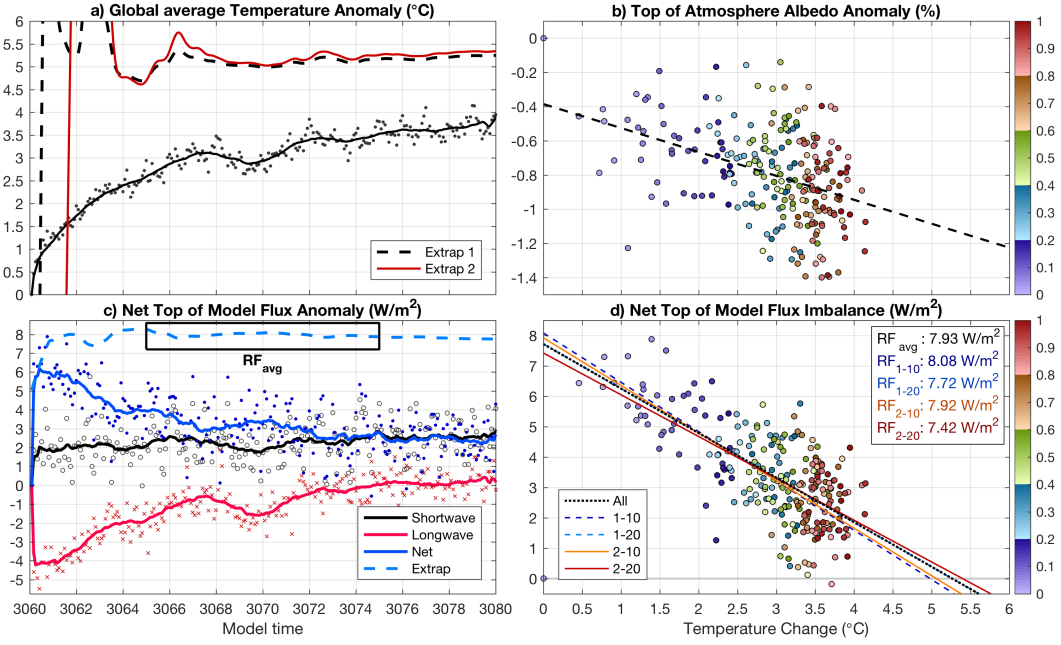

Figure S17. First 20 years of the response after an instant quadrupling of atmospheric CO_2, starting from the equilibrated state of the pre-industrial reference. Model years 3060–3080 for both the reference and 4×CO_2 simulations are considered, of which the monthly mean output fields are compared 1 on 1. The respective differences are shown for monthly mean, globally average **a)** near surface air temperature, **b)** top of the atmosphere albedo, **c)** top of model net shortwave (black), longwave (red) and net (blue) flux, and **d)** top of model net flux imbalance versus temperature. In addition to monthly means (dots in a), c); markers in b), d) coloured to normalised model time), smoothing averages are shown using a 2-year sliding window. A simple linear regression is added using a dashed black line in b), d) with the latter including the results of different time intervals and the corresponding estimated radiative forcing. The progression of the estimated fast equilibrium temperature response using a linear regression starting from year 1 (dashed black) and year 2 (solid red) is shown is shown as well in a), the same is done for the radiative forcing in c) (dashed blue; from year one only). The radiative forcing experienced by the model in this perturbation experiment is estimated by taking the mean of all extrapolations using years 1–6 to 1–15 (i.e. 3066 to 3075) and shown as RF_{avg} in d).

Sea surface temperature proxies

42–38 Ma SST Proxies:

Site	p-lat	p-lon	SST (°C)	σ (°C)	Reference	Method
DSDP 277	-55.5	178.1	28	4.7	Hines et al. (2017)	Mg/Ca
ODP 865	11.8	-147.0	31	4.7	Tripati et al. (2003)	Mg/Ca
ODP 925	3.5	-30.9	32	2.5	Liu et al. (2009)	TEX_{86}^{H}
ODP 929	-1.8	-31.2	30	2.5	Liu et al. (2009)	TEX_{86}^{H}
ODP 959	-5.23	-2.59	31.5	2.5	Cramwinckel et al. (2018)	TEX_{86}^{H}
ODP 1052	24.2	-61.6	32	1.2	Okafor et al. (2009)	Mg/Ca
ODP 1172	-57.8	157.9	24	2.5	Bijl et al. (2009)	TEX_{86}^{H}
ACEX	82.5	-5.7	10	2.7	Evans et al. (2018)	UK_{37}
Gulf Coast, US	28.3	-74.1	26	1.4	Kobashi et al. (2004)	$\delta^{18}O$
Istra More 5	34.1	13.1	24	0.7	Pearson et al. (2001)	$\delta^{18}O$
Java KW01	0.1	114.5	35	2.0	Evans et al. (2018)	Δ_{47}
			36.3	1.9	Evans et al. (2018)	Δ_{47}
New Zealand	-49.3	-169.7	26	4.7	Hines et al. (2017)	Mg/Ca
Seymour Is.	-68.5	-62.5	12.7	2.4	Douglas et al. (2014)	Δ_{47}
			13.1	2.4	Douglas et al. (2014)	Δ_{47}
			20.3	2.5	Douglas et al. (2014)	TEX_{86}^{H}
Tanzania	-16.6	40.6	34	2.5	Pearson et al. (2007)	TEX_{86}^{H}
Tanz. Lindi	-17.6	40.6	32	0.7	Pearson et al. (2001)	$\delta^{18}O$
Hamp. Bas., UK	43.6	-2.9	23.2	2.6	Evans et al. (2018)	Δ_{47}

Table S3. Overview of 42–38 Ma SST proxies; site location, 38Ma reconstructed coordinates (p-lat,p-lon), SST estimate, calibration error, reference and method used.

38–34 Ma SST Proxies:

Site	p-lat	p-lon	SST (°C)	σ (°C)	Reference	Method
DSDP 277	-55.5	178.1	26.6	2.5	Liu et al. (2009)	TEX_{86}^{H}
			25.6	4.7	Liu et al. (2009)	UK_{37}
DSDP 336	55.7	-11.0	20	1.5	Liu et al. (2009)	UK_{37}
DSDP 511	-58.8	-30.4	19.5	2.5	Liu et al. (2009)	TEX_{86}^{H}
			19.6	1.5	Liu et al. (2009)	UK_{37}
ODP 689	-68.3	14.0	12.3	4.6	Petersen and Schrag (2015)	Δ_{47}
			22.0	1.5	Petersen and Schrag (2015)	Δ_{47}
ODP 803	-0.8	-169.1	27.4	2.5	Liu et al. (2009)	TEX_{86}^{H}
ODP 913	66.2	-2.4	18.3	1.5	Liu et al. (2009)	UK_{37}
ODP 925	3.5	-30.9	30	2.5	Liu et al. (2009)	TEX_{86}^{H}
ODP 929	-1.8	-31.2	29	2.5	Liu et al. (2009)	TEX_{86}^{H}
ODP 959	-5.23	-2.59	28.5	2.5	Cramwinckel et al. (2018)	TEX_{86}^{H}
ODP 998	14.6	-69.4	22.1	2.5	Liu et al. (2009)	TEX_{86}^{H}
ODP 1052	24.2	-61.6	30	1.2	Okafor et al. (2009)	Mg/Ca
ODP 1090	-51.9	157.9	22	2.5	Bijl et al. (2009)	UK_{37}
ODP 1172	-57.8	157.9	22	2.5	Bijl et al. (2009)	TEX_{86}^{H}
Alabama, US	27.6	-72.4	27	0.7	Pearson et al. (2001)	$\delta^{18}O$
Browns C., Aus	-53.8	147.2	18.9	0.7	Kamp et al. (1990)	$\delta^{18}O$
Gulf Coast, US	28.3	-74.1	22	1.4	Kobashi et al. (2004)	$\delta^{18}O$
New Zealand	-49.3	-169.7	30.9	4.7	Hines et al. (2017)	Mg/Ca
Panama	0.9	-72.9	32	1.4	Tripati and Zachos (2002)	$\delta^{18}O$
Seymour Is.	-68.5	-62.5	12.2	2.4	Douglas et al. (2014)	Δ_{47}
			13.0	3.0	Douglas et al. (2014)	Δ_{47}
			16.0	2.5	Douglas et al. (2014)	TEX_{86}^{H}
St Stephens Q.	27.2	-72.2	32.5	2.2	Wade et al. (2012)	Mg/Ca
			34.9	4.7	Wade et al. (2012)	Mg/Ca
			30.5	2.5	Wade et al. (2012)	TEX_{86}^{H}
Tanzania	-16.6	40.6	29.5	0.7	Pearson et al. (2007)	$\delta^{18}O$
			33.0	2.5	Pearson et al. (2007)	TEX_{86}^{H}
			29.7	3.2	Evans et al. (2018)	Δ_{47}
Tanz. Lindi	-17.6	40.6	30.0	0.7	Pearson et al. (2001)	$\delta^{18}O$

Table S4. Overview of 38–34 Ma SST proxies; site location, 38Ma reconstructed coordinates (p-lat,p-lon), SST estimate, calibration error, reference and method used.

Terrestrial Temperature Proxies

Late Middle Eocene Land Temperature Proxies:

Site	T_a (°C)	T_x (°C)	T_n (°C)	p-lat	p-lon	Reference
North Atlantic:						
ODP 913 MBT	14.5	16.0	12.5	66.2	-2.4	Schouten et al. (2008)
ODP 913 Pollen	13.3	16.2	11.8	66.2	-2.4	Eldrett et al. (2009)
North America:						
Florissant CO	14.6	17.5	10.7	37.0	-86.9	Boyle et al. (2008)
Comstock (OR)	21	22.4	19.6	44.7	-102.9	Retallack et al. (2004)
Copper B. (NV)	9.5	10.5	8.5	41.5	-96.0	Wolfe et al. (1998)
Badger's N. (CA)	14.5	17.1	12.5	42.1	-100.6	Prothero (2008)
Sevier (UT)	13.2	13.2	13.2	38.7	-94.7	Gregory-Wodzicki (1997)
Gray B. (OR)	14.0	19.3	8.8	45.0	-100.6	Smith et al. (1998)
South America:						
Ñirihuau (Chile)	18.4	18.4	18.4	-49.4	-59.5	Hinojosa and Villagrán (2005)
Europe:						
Stare Sedlo	23.9	29	21.3	43.7	9.3	Uhl et al. (2007)
Weiße Elster	22.6	24	18.7	44.9	8.3	Uhl et al. (2007)
China:						
Dalianhe	16.5	16.5	16.5	54.2	129.1	Quan et al. (2012)
Huanghua	18.1	18.3	17.9	52.7	129.4	Quan et al. (2012)
Jushu	15.9	16.1	15.6	52.4	126.5	Quan et al. (2012)
Hunchun	17.5	18.4	16.5	50.8	130.9	Quan et al. (2012)
Huadian	17.0	18.4	15.6	50.8	126.4	Quan et al. (2012)
Jijuntun	16.8	17	16.5	49.6	123.3	Quan et al. (2012)
Xilutan	17.0	18.4	15.6	49.6	123.3	Quan et al. (2012)
Kongdian	17.5	18.4	16.5	47.4	118.7	Quan et al. (2012)
Shahejie	17.1	18.4	15.7	45.6	116.3	Quan et al. (2012)
Sanduo	17.1	18.4	15.7	40.7	118.4	Quan et al. (2012)
Dingyuan	15.5	16.1	14.8	39.6	116.1	Quan et al. (2012)
Shuangta	16.1	16.4	15.7	38.8	117.9	Quan et al. (2012)
Qingjiang	16.5	16.5	16.5	35.5	115.5	Quan et al. (2012)
Wenzhou	17.6	18.4	16.8	34.6	121.8	Quan et al. (2012)
Tantou	17.1	18.4	15.7	40.7	110.7	Quan et al. (2012)

Table S5. Overview of late middle Eocene terrestrial temperature proxies; site location, mean annual temperature, highest annual temperature, lowest annual temperature and 38Ma reconstructed coordinates.

Site	T_a (°C)	T_x (°C)	T_n (°C)	p-lat	p-lon	Reference
Unnamed Unit 1	15.9	18.4	13.3	45.6	105.8	Quan et al. (2012)
Unnamed Unit 2	13.7	16.1	11.3	42.5	101.8	Quan et al. (2012)
Honggou	17.2	21.1	13.3	42.6	99.9	Quan et al. (2012)
Relu	14.1	16.4	11.7	36.3	95.1	Quan et al. (2012)
Huoshaogou	16.4	21.7	11.0	45.4	93.7	Quan et al. (2012)
Lulehe	17.1	18.4	15.7	41.2	86.0	Quan et al. (2012)
Lulehe	17.1	18.4	15.7	37.0	88.1	Quan et al. (2012)
Totohe	14.9	16.5	13.3	34.6	87.3	Quan et al. (2012)
Wulagen	18.2	20.8	15.6	39.3	74.4	Quan et al. (2012)
Shenhu	16.6	21.7	11.5	30.0	113.3	Quan et al. (2012)
Liushagang	17.6	23.9	11.3	28.1	109.7	Quan et al. (2012)
Changchang	18.9	20.8	17	26.8	110.6	Quan et al. (2012)
Australia:						
Anglesea	16.2	19.3	13.9	-53.4	148.2	Greenwood et al. (2004)
Hasties	16.2	16.2	16.2	-55.3	153.8	Greenwood and Wing (1995)
West Dale	16.1	17.9	14.2	-49.1	111.4	Greenwood et al. (2004)
Antarctica:						
McMurdo	13.0	13.0	13.0	-72.1	158.2	Passchier et al. (2013)
SA Islands AP	12.0	15.0	10.5	-67.5	-63.5	Passchier et al. (2013)

Table S5. Continued.

Late Eocene Land Temperature Proxies:

Site	T_a (°C)	T_x (°C)	T_n (°C)	p-lat	p-lon	Reference
North Atlantic:						
ODP 913 MBT	14.0	15.9	7.9	66.2	-2.4	Schouten et al. (2008)
ODP 913 Pollen	13.4	16.2	11.8	66.2	-2.4	Eldrett et al. (2009)
North America:						
Florissant CO	14.6	17.5	10.7	37.0	-86.9	Boyle et al. (2008)
Comstock (OR)	21	22.4	19.6	44.7	-102.9	Retallack et al. (2004)
Copper B. (NV)	9.5	10.5	8.5	41.5	-96.0	Wolfe et al. (1998)
Badger's N. (CA)	14.5	17.1	12.5	42.1	-100.6	Prothero (2008)
Sevier (UT)	13.2	13.2	13.2	38.7	-94.7	Gregory-Wodzicki (1997)
Gray B. (OR)	14.0	19.3	8.8	45.0	-100.6	Smith et al. (1998)

Table S6. Overview of late Eocene terrestrial temperature proxies; site location, mean annual temperature, highest annual temperature, lowest annual temperature and 38Ma reconstructed coordinates.

Site	T_a (°C)	T_x (°C)	T_n (°C)	p-lat	p-lon	Reference
South America:						
Ñirihuau (Chile)	18.4	18.4	18.4	-49.4	-59.5	Hinojosa and Villagrán (2005)
Europe:						
Stare Sedlo	23.9	29	21.3	43.7	9.3	Uhl et al. (2007)
Weiße Elster	22.6	24	18.7	44.9	8.3	Uhl et al. (2007)
China:						
Hunchun	18.2	18.4	17.9	50.8	130.9	Quan et al. (2012)
Gengjiajie	18.2	18.4	17.9	49.6	123.3	Quan et al. (2012)
Shahejie	17.5	18.4	16.5	47.4	118.7	Quan et al. (2012)
Sanduo	18.2	20.8	15.6	40.7	118.4	Quan et al. (2012)
Dingyuan	13.9	16.1	11.6	39.6	116.1	Quan et al. (2012)
Linjiang	18.0	19.4	16.5	35.5	115.5	Quan et al. (2012)
Pinghu	17.0	18.4	15.6	34.6	121.8	Quan et al. (2012)
Unnamed Unit 2	14.1	16.5	11.6	42.5	101.8	Quan et al. (2012)
Honggou	17.2	21.1	13.3	42.6	99.9	Quan et al. (2012)
Relu	15.2	15.6	14.8	36.3	95.1	Quan et al. (2012)
Huoshaogou	15.6	21.7	9.4	45.4	93.7	Quan et al. (2012)
Xiaganchaigou	17.1	18.4	15.7	41.2	86.0	Quan et al. (2012)
Wanbaogou	19.2	21.9	16.5	37.0	88.1	Quan et al. (2012)
Bashibulake	17.1	20.8	13.3	39.3	74.4	Quan et al. (2012)
Xiaokuzibai	18.8	20.8	16.8	43.8	78.7	Quan et al. (2012)
Youganwo	17.2	18.6	15.7	28.6	110.8	Quan et al. (2012)
Liushagang	16.1	20.8	11.3	28.1	109.7	Quan et al. (2012)
Yongning Gr.	17.8	18.4	17.2	28.8	106.8	Quan et al. (2012)
Nadu	15.9	16.1	15.7	30.5	106.0	Quan et al. (2012)
Dagzhuka	17.5	18.4	16.5	29.9	87.6	Quan et al. (2012)
Antarctica:						
McMurdo	13.0	13.0	13.0	-72.1	158.2	Passchier et al. (2013)
King George	13.4	15.0	11.7	-66.3	-64.5	Passchier et al. (2013)
ODP 1166	12.0	12.0	12.0	-64.8	87.3	Passchier et al. (2013)

Table S6. Continued.